Solid Iron Compressed Up to 560 GPa

Y. Ping, F. Coppari, D. G. Hicks, B. Yaakobi, D. E. Fratanduono, S. Hamel, J. H. Eggert, J. R. Rygg, R. F. Smith, D. C. Swift, D. G. Braun, T. R. Boehly, and G. W. Collins

Phys. Rev. Lett. **111**, 065501 — Published 5 August 2013

DOI: 10.1103/PhysRevLett.111.065501

Solid iron compressed up to 560 GPa

Y. Ping[1], F. Coppari[1], D. G. Hicks[1], B. Yaakobi[2], D. E. Fratanduono[1], S. Hamel[1], J. H. Eggert[1], J. R. Rygg[1], R. F. Smith[1], D. C. Swift[1], D. G. Braun[1], T. R. Boehly[2], and G. W. Collins[1]
[1]*Lawrence Livermore National Laboratory, Livermore, CA and*
[2]*Laboratory for Laser Energetics, University of Rochester, Rochester, NY*

Dynamic compression by multiple shocks is used to compress iron up to 560 GPa (5.6 Mbar), the highest solid-state pressure yet attained for iron in the laboratory. EXAFS (extended x-ray absorption fine structure) spectroscopy offers simultaneous density, temperature and local-structure measurements for the compressed iron. The data show that the close-packed structure of iron is stable up to 560 GPa, the temperature at peak compression is significantly higher than expected from pure compressive work, and the dynamic strength of iron many times greater than the static strength based on lower pressure data. The results provide the first constraint on the melting line of iron above 400 GPa.

PACS numbers: 62.50.-p, 61.05.cj, 91.45.Bg, 64.70.kd

Material properties at high-energy-density conditions are of broad interest across several scientific fields [1, 2], from geophysics, planetary science, to laboratory astrophysics as well as inertial confinement fusion. Iron (Fe) is a key constituent of terrestrial planets and exoplanets, and the sixth most abundant element in the Universe, thus is one of the most studied materials under extreme conditions. Theoretical calculations have made many predictions on Fe structures [3–8], melting line [9, 10], elasticity [11–17] and conductivity [18] at elevated pressures and temperatures. Recently, the theoretical phase diagram of Fe has been extended up to 100 TPa and 40,000 K [19]. However, experimental data on solid Fe are reported only up to 370 GPa [20–23]. Measurements at higher pressures represent a challenging frontier in material science, which can impact the development of evolution models for exoplanets [24]. The lack of data has left the theoretical models and predictions untested in the pressure regime beyond the Earth core conditions.

In this Letter we report measurements of solid Fe compressed up to 560 GPa, providing the highest-pressure data to date for constraining these models. The data demonstrate a close-packed structure of solid Fe up to 560 GPa, and provide the first constraint on the melting line of Fe above 400 GPa. The temperature at peak compression is substantially higher than expected from compressive work, indicating an enhanced strength of Fe under our experimental conditions.

The record pressure on Fe is achieved by dynamic ramp compression, where the pressure history is tuned to follow a particular path. This technique was recently used to explore solid diamond to 800 GPa [25]. In contrast to single-shock compression where the states are all along the Hugoniot, ramp or multi-shock compression can achieve off-Hugoniot states with lower temperatures. Hence, materials can maintain a solid structure while being compressed into TPa regime.

Diagnosing the material properties under extreme conditions is as important as the creation of high-pressure states. We have performed EXAFS (extended x-ray absorption fine structure) measurements on the compressed Fe, providing *in situ* density, temperature and local-structure data. EXAFS refers to the oscillatory modulations in x-ray absorption spectra above an absorption edge, which are generated by interference between photo-electron waves and scattering by neighbor atoms [26]. The period of the modulations depends primarily on the nearest-neighbor distance, from which the density can be determined. The decay of the modulations at higher x-ray energies is set by the Debye-Waller factor (DWF) [27], from which the temperature can be determined. EXAFS has been employed to study dynamically compressed Fe up to 35 GPa [28]. Here we extend the measurements to much higher pressures by taking into account anharmonic effects [29–31].

The experiments were performed on the OMEGA laser system at Laboratory for Laser Energetics (LLE). As shown in Fig. 1(a), a broadband x-ray backlighter was generated by a spherical implosion [28, 32]. The target was a $4\mu m$-thick Fe foil (purity better than 99.99%) sandwiched between two diamond plates, each $35\mu m$ thick. The diamond played a similar role as in the diamond anvil cell: confining the sample and maintaining the pressure, thus creating a spatially uniform compression state in Fe. The driver consists of five stacked laser pulses, and a typical pulse shape is plotted in Fig. 1(b). The corresponding stress history in Fe, obtained by velocimetry as described below, is plotted in Fig. 1(c). Both the laser energy and the delay between the driver and the backlighter were varied in order to probe different pressures and temperatures.

The stress in Fe is obtained from measurements of the free surface velocity of diamond using a line-imaging VISAR (velocity interferometer system for any reflector) [33]. The 532-nm VISAR probe was directed onto the target by a mirror integrated into the target package. The mirror also shields the target from the implosion, and its presence has minimal effect on the EXAFS measurements. The method of characteristics [34] was used to backwards propagate the free surface velocity to determine the history of normal stress at the iron-diamond interface using a measured diamond equation of state [25].

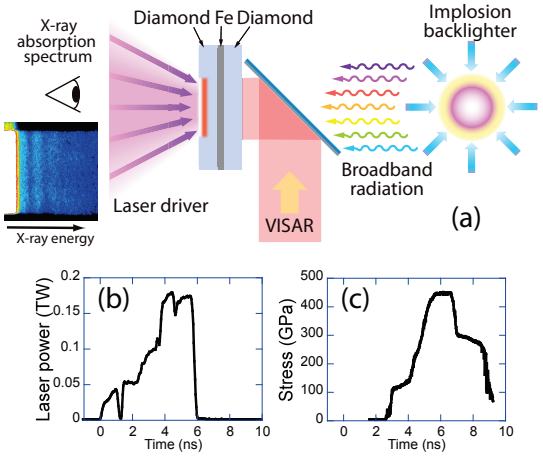

FIG. 1: (a) Experimental schematic. A raw image of a typical x-ray absorption spectrum is displayed at the left-lower corner, showing the intensity modulations above the K-edge. (b) A typical laser pulse shape of the drive formed by five 1ns laser pulses stacked in time. (c) The stress in Fe obtained from velocimetry measurements for the pulse shape in (b).

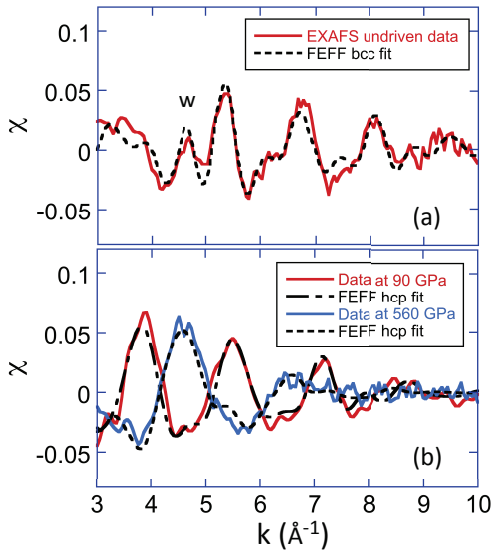

FIG. 2: (a) EXAFS data at ambient conditions and FEFF bcc fit. (b) EXAFS data at 90 GPa and 560 GPa, with corresponding FEFF fitting results.

The Fe thickness was substantially thinner than the diamond sandwich such that the pressure in the Fe sample equilibrates with that of the diamond. The pressure equilibration is confirmed by hydrodynamic simulations using LASNEX [35]. The short duration of the x-ray backlighter (∼120 ps) [32] ensures little temporal variation in the state of Fe during EXAFS measurements.

The normalized EXAFS signal, $\chi(k) = \mu(k)/\mu_0(k) - 1$, for undriven and compressed Fe are shown in Fig. 2(a) and (b), respectively (μ_0 is the smooth atomic-like absorption coefficient, k is the wave number). At ambient conditions, Fe has body-centered cubic (bcc) structure and the data agree well with both synchrotron measurements and calculations using FEFF code [26] (Fig. 2a). Fe is known to undergo a phase transition from bcc to hcp (hexagonal close-packed) at pressures above 13 GPa [36, 37]. The disappearance of the "w" peak is a signature of the phase transition [28] as shown in Fig. 2(b). The spectra of compressed Fe are fitted well with FEFF calculations of hcp lattice (c/a= 1.60) using IFEFFIT program [38] including the third cumulant to take into account the anharmonic effect. Variation of c/a ratio in the range of 1.59-1.63 as determined in diffraction measurements [20] has negligible effect on the inferred density and temperature.

Since simulations [3–8, 19] suggest existence of hcp, bcc or fcc phases at high pressures and high temperatures, we performed first-principle quantum molecular dynamics (QMD) simulations to create bcc, hcp, fcc as well as liquid atomic configurations of Fe to compare the difference in EXAFS spectra [39]. EXAFS measurements will not discriminate between close-packed phases including hcp, fcc and dhcp as they display similar EXAFS signals [8]. In the following data analysis, we use hcp to represent close-packed structures. The pair distribution function g(r) from the QMD simulations, shown in Fig. 3(a), indicates that at high temperatures, the first two shells of the bcc lattice are merged into a broader peak, which resembles the first peak in g(r) of an hcp lattice. However, at the same density the nearest-neighbor distance, R_1, in bcc is ∼3% shorter than that in hcp, and thus the resulting EXAFS signal is shifted for hot bcc relative to hcp. Therefore, fitting the same data with the hot bcc lattice results in ∼10% reduction in density compared to hcp fitting. The liquid phase, characterized by an even broader and more shifted first peak in g(r), leads to even lower densities than bcc in the data fitting.

The compression obtained from EXAFS data as a function of stress is plotted in Fig. 3(b). The density is determined from R_1 which is obtained by fitting EXAFS data using four types of lattice structures: harmonic hcp, anharmonic hcp, bcc and liquid generated by the QMD simulations. In the same figure the Fe Hugoniot [40] and principle isentrope from LEOS library [41] are also shown for comparison. For the multi-shock compression, the density should lie between the Hugoniot and the isentrope. Clearly the anharmonic correction is necessary to obtain the correct density for the hcp phase. The bcc and liquid fittings give lower density at the same stress as explained above, which is too low compared to the Hugoniot for all the data. Therefore, the fitting results indicate that our EXAFS data are inconsistent with the bcc and liquid phases.

The experimental EXAFS data were also analyzed using an independent approach implemented in the GNXAS package [42]. This approach is based on relating g(r) to $\chi(k)$, a well-established procedure developed for disordered systems. Coordination numbers of the first shell obtained from data fitting are shown in Fig. 3(c) as a function of stress. From 90 to 560 GPa, the average value of best-fit N_1 is ∼11±1, close to the expected co-

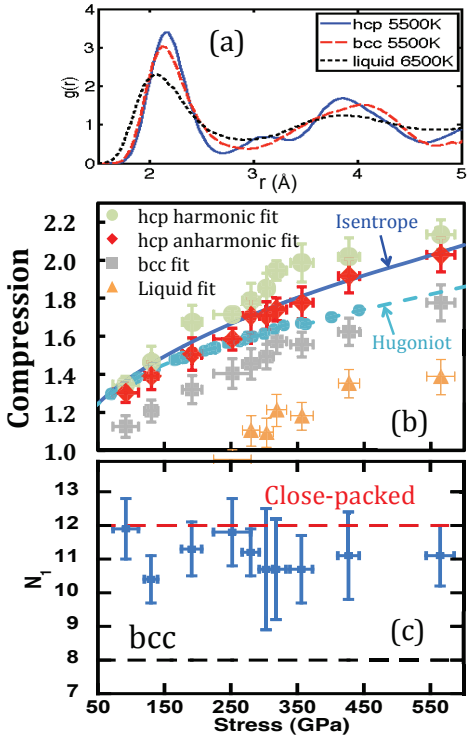

FIG. 3: (a) g(r) from QMD simulations for bcc, hcp and liquid at 1.575× compression. (b) Compression as a function of stress for four types of FEFF fitting of EXAFS data, together with Hugoniot data [40] and the principle isentrope [41]. The fitting of undriven data gives a compression of 1.01±0.02. (c) Best-fit first-shell coordination number using GNXAS.

ordination number of a close-packed structure ($N_1 = 12$, red dashed line) but far from the bcc lattice ($N_1 = 8$, black dashed line). Therefore, both FEFF and GNXAS fitting of EXAFS data are consistent with a close-packed structure rather than the bcc phase. The fact that the observed coordination number is slightly less than the ideal value for a close-packed structure could be due to microstructural defects [43] or significant thermal vibrations at such high temperatures. The σ^2 obtained from these two independent methods are also in good agreement [39].

The temperature dependence of EXAFS occurs through the DWF, σ^2 [43–46]. Since EXAFS measures the inter-atom distances, the correlation effect in atomic motion should be taken into account [27]. The correlated Einstein model and Debye model with harmonic approximation are commonly used to calculate σ^2, and generally produce similar results [31]. Taking into account the anharmonic effect in the Einstein model to the lowest order, in the high-temperature limit we get [39]

$$\sigma^2 = \sigma_E^2(T) + (\sigma_3/\sigma_E^2(T))^2 \quad (1)$$

where σ_3 is the third cumulant, and σ_E^2 is from the harmonic Einstein model, $\sigma_E^2 = \frac{\hbar}{M\omega_E}\coth(\frac{\hbar\omega_E}{2k_BT})$ (M is the atomic mass, ω_E is the Einstein frequency, $\hbar$ is the Planck constant, k_B is the Boltzmann constant). The second term in Eq. (1) represents the lowest-order anharmonic contribution. The Einstein temperature is given by $T_E = \frac{3}{4}T_{Debye}$ for the first shell [27], with T_{Debye} extrapolated from experimental measurements of Fe up to 300 GPa [21]. The validity of Eq. (1) has been confirmed using synthetic EXAFS data from QMD simulations [39].

The temperature obtained from DWF in EXAFS data using Eq. (1) is plotted in Fig. 4(a) and (b) as a function of stress. The relatively large error bars are due to the fact that at such high temperatures, the EXAFS signal is damped strongly at higher k, and hence only a limited number of peaks are observable as shown in Fig. 2(b). Nevertheless, the data clearly indicate that off-Hugoniot states have been achieved up to 560 GPa and 8000 K, which are the highest stress and temperature ever reached for solid iron. The data fall into three groups based on the compression history: single shock (blue diamonds), first shock stress P_1= 80-100 GPa shown in Fig. 4(a) (red squares) and P_1= 130-150 GPa shown in Fig. 4(b) (black triangles). The two single-shock points agree well with the calculated Hugoniot. The multi-shock data show the expected higher temperature at higher P_1, but compared to the isentropes calculated following 100 and 150 GPa initial shock as plotted in Fig. 4 (a) and (b) respectively (solid lines), our inferred temperatures are 1000-4000 K higher.

The temperature can result from processes such as x-ray preheat by either the laser driver or the backlighter, thermal conduction from diamond to Fe, shock heating, and heating due to work against the strength of Fe during the high strain rate compression (plastic work). EXAFS measurements of undriven targets as plotted in Fig. 2(a) gives a temperature of $310\pm70K$, indicating that heating by the backlighter is negligible. We have performed radiation hydrodynamic simulations to estimate the x-ray heating by the driver and the thermal conduction. Both are much smaller than shock heating and plastic work. The contribution due to shock heating after the initial shock is also expected to be small because the subsequent compression is either shockless or consists of weak shocks with little additional entropy. The major contribution to the temperature is thus mainly due to heating by the first shock and the plastic work. The latter can be expressed as [47]:

$$\Delta T_{plastic} = \frac{V_0}{C_V}\int_{\eta_1} Y(\eta)\frac{d\varepsilon}{d\eta}d\eta \quad (2)$$

where ε is the plastic strain, $\varepsilon = \frac{2}{3}[\ln(\eta) - Y/(2G)]$, Y is the strength, G is the shear modulus, C_V is the specific heat, $\eta = \rho/\rho_0$, ρ is the density, V_0 and ρ_0 are the volume and the density at ambient conditions, and η_1 is the compression by the first shock. The Dulong-Petit limit is used for the heat capacity, $C_V \simeq 3k_B$, as the temperature already reaches above 3000 K for off-Hugoniot data after the first shock. We used a density- and temperature-dependent shear modulus G based on Ref. [11], but the

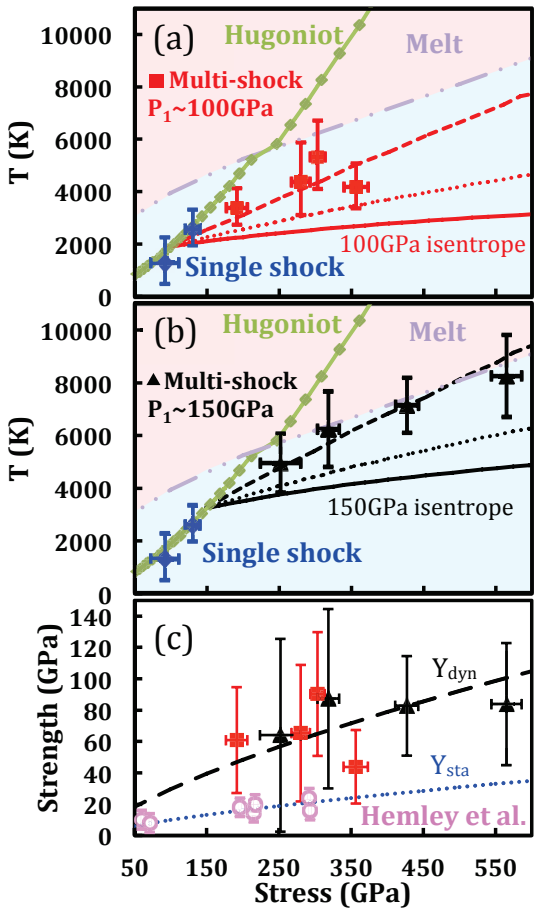

FIG. 4: (a) and (b) Temperature inferred from DWF in EXAFS data using Eq. (1) as a function of stress for the two groups of multi-shock data with an initial shock of ∼100 GPa and ∼150 GPa, respectively. The single-shock data are also shown (blue diamonds). The melting curve [9] (dot-dot-dashed lines) and the Hugoniot [41] (green solid lines with dots) are plotted for comparison. Also shown are isentropes (solid lines), isentropes with the temperature increase calculated using Y_{sta} (dotted lines) and $Y_{dyn} = 3Y_{sta}$ (dashed lines). (c) Fe strength vs. stress from our data (red squares and black triangles) and static data (circles) [22].

choice of G [11–17] does not significantly affect the results because in the expression of $\frac{d\varepsilon}{d\eta}$, $\frac{d}{d\eta}(\frac{Y}{2G}) \ll \frac{d}{d\eta}\ln(\eta)$ under our conditions. For the strength of Fe, the published data up to 300 GPa by static compression (Y_{sta}) are generally considered as the lower limit due to deformation of diamond anvils [22]. The data trend is extrapolated to 600 GPa as shown in Fig. 4(c) (dotted line). The plastic work calculated using Y_{sta} leads to ∼ 500-1500 K temperature increase as shown in Fig. 4(a) and (b) (dotted line), which is close to the lower limit of our data.

This substantial plastic heating indicates that the strength of Fe is much higher than expected from lower-pressure static data. The upper limit of the dynamic strength, Y_{dyn}, for our compression path can be estimated by attributing the difference between the experimental temperature and the calculated isentrope temperature to the plastic work. The temperature rise using an assumed dynamic strength, $Y_{dyn} = 3Y_{sta}$, is shown by the dashed lines in Fig. 4(a) and (b), which, on the average, is consistent with both groups of data. Comparison of Y_{dyn} from our multi-shock data and Y_{sta} from static data is shown in Fig. 4(c). Besides the fact that the static experiments give a lower limit on the strength due to anvil deformation, the difference between Y_{dyn} and Y_{sta} can also arise from the commonly observed increase in strength at high strain rates [48]. One uncertainty in setting Y_{dyn} lies in the fraction of plastic work converted into heat, the Taylor-Quinney factor β [49]. In the above calculations, β is assumed to be 100%. Recent experiments have shown that as the strain rate is increased from $3.8 \times 10^3 s^{-1}$ to $8.4 \times 10^3 s^{-1}$, β rises from ∼50% to ∼100% [50]. However, there are no measurements or calculations on β so far for strain rates on the order of $10^6 - 10^7 s^{-1}$ as in our experiments, thus our data effectively constrain the upper limit of the product βY.

To summarize, EXAFS measurements have provided density, temperature, and local-structure data for Fe compressed up to 560 GPa. By comparing with QMD simulations, the data are consistent with a close-packed solid structure rather than a bcc or liquid phases. The high temperature at peak compression is interpreted to be due to the dynamic strength of Fe, which for the compression history explored here, is several times greater than expected from lower pressure static data. The platform developed for EXAFS study of Fe can be applied to many solids at pressures well into the TPa regime, which is accessible by ramp/multi-shock compression using National Ignition Facility [51].

We wish to thank the OMEGA team at LLE for laser operation and technical support. We also would like to thank W. Unites, T. Uphaus, S. Uhlich and R. Wallace for target fabrication. We appreciate helpful discussion with R. E. Rudd and R. Kraus. Y.P. acknowledges support from DOE HEDLP program. This work was performed under the auspices of U. S. DOE by LLNL under contract number DEAC52-07NA27344 and the LDRD program at LLNL.

[1] National Research Council (U.S.) Committee on High Energy Density Physics, *Frontiers in High Energy Density Physics: The X-Games of Contemporary Science* (National Academies Press, Washington, DC, 2003).
[2] Report of the Workshop on High Energy Density Laboratory Physics Research Needs, DOE Office of Science and NNSA (Nov. 2009).
[3] A. B. Belonoshko, R. Ahuja and B. Johansson, Nature **424**, 1032 (2003).
[4] Y. Kuwayama, K. Hirose, N. Sata, Y. Ohishi, Earth

Planet. Sci. Lett. **273**, 379 (2008).
[5] T. Sakai, E. Ohtani, N. Hirao and Y. Ohishi, Geophys. Res. Lett. **38**, L09302 (2011).
[6] L. Vocadlo, I. G. Wood, D. Alfe and G. D. Price, Earth Planet. Sci. Lett. **268**, 444 (2008).
[7] A. S. Mikhaylushkin, *et al.* Phys. Rev. Lett. **99**, 165505 (2007).
[8] K. Kadau, *et al.* Phys. Rev. Lett. **98**, 135701 (2007).
[9] D. Alfe, G. D. Price and M. J. Gillan, Phys. Rev. B **65**, 165118 (2002); D. Alfe, Phys. Rev. B **79**, 060101 (2009).
[10] A. B. Belonoshko, R. Ahuja, and B. Johansson, Phys. Rev. Lett. **84**, 3638 (2000).
[11] X. Sha and R. E. Cohen, Phys. Rev. B **81**, 094105 (2010).
[12] R. E. Cohen, L. Stixrude and E. Wasserman, Phys. Rev. B **56**, 8575 (1997).
[13] A. Laio, S. Bernard, G. L. Chiarotti, S. Scandolo, E. Tosatti, Science **287**, 1027 (2000).
[14] G. Steinle-Neumann, L. Stixrude, R. E. Cohen and O. Gulseren, Nature **424**, 1032 (2003).
[15] D. Alfe, G. D. Price and M. J. Gillan, Phys. Rev. B **64**, 045123 (2001).
[16] L. Vocadlo, D. P. Dobson and I. G. Wood, Earth Planet. Sci. Lett. **288**, 534 (2009).
[17] A. B. Belonoshko, T. Bryk, and A. Rosengren, Phys. Rev. Lett. **104**, 245703 (2010).
[18] M. Pozzo, C. Davis, D. Gubbins and D. Alfe, Nature **485**, 355 (2012).
[19] L. Stixrude, Phys. Rev. Lett. **108**, 055505 (2012).
[20] S. Tateno, K. Hirose, Y. Ohishi and Y. Tatsumi, Science **330**, 359 (2010).
[21] L. S. Dubrovinsky, S. K. Saxena, N. A. Dubrovinskaia, S. Rekhi and T. Le Bihan, Am. Minerals **85**, 386 (2000).
[22] R. J. Hemley, H. Mao, G. Shen, J. Badro, P. Gillet, M. Hanfland, D. Hausermann, Science **276**, 1242 (1997).
[23] S. Anzellini, A. Dewaele, M. Mezouar, P. Loubeyre, G. Morard, Science **340**, 464 (2013).
[24] D. C. Swift, *et al.* Astrophys. J. **744**, 59 (2012).
[25] D. K. Bradley, *et al.* Phys. Rev. Lett. **102**, 075503 (2009).
[26] J. J. Rehr and R. C. Albers, Rev. Mod. Phys. **72**, 621 (2000).
[27] E. Sevillano, H. Meuth and J. J. Rehr, Phys. Rev. B **20**, 4908 (1979).
[28] B. Yaakobi, *et al.* Phys. Rev. Lett. **95**, 075501 (2005).
[29] J. M. Tranquada and R. Ingalls, Phys. Rev. B **28**, 3520 (1983).
[30] E. A. Stern, P. Livins and Z. Zhang, Phys. Rev. B **43**, 8850 (1991).
[31] K. D. Machadoa, J. Chem. Phys. **134**, 064503 (2011).
[32] B. Yaakobi, F. J. Marshall, T. R. Boehly, R. P. J. Town and D. D. Mayerhofer, J. Opt. Soc. Am. B **20**, 238 (2003).
[33] P. M. Celliers, *et al.* Rev. Sci. Instrum. **75**, 4916 (2004).
[34] S. D. Rothman and J. Maw, J. Phys. IV France **134**, 745 (2006).
[35] G. B. Zimmerman and W. L. Kruer, Comments on Plasma Phys. Contr. Fusion **2**, 51 (1975).
[36] D. H. Kalantar, *et al.* Phys. Rev. Lett. **95**, 075502 (2005).
[37] T. Takahashi, W. A. Bassett, Science **145**, 483 (1964); W. A. Bassett, E. Huang, Science **238**, 780 (1987).
[38] B. Ravel and M. J. Newville, Synchrotron Rad. **12**, 537 (2005).
[39] See Supplemental Materials.
[40] J. M. Brown, J. N. Fritz and R. S. Hixson, J. Appl. Phys. **88**, 5496 (2000).
[41] LEOS data library is based on a QEOS-like model described in: R. M. More, K. H. Warren, D. A. Young and G. B. Zimmerman, Phys. Fluids **31**, 3059 (1988); D. A. Young and E. M. Corey, J. Appl. Phys. **78**, 3748 (1995).
[42] A. Filipponi, A. Di Cicco, Phys. Rev. B **52**, 15135 (1995); A. Filipponi, J. Phys: Cond. Matt. **6**, 8415 (1994).
[43] A. Di Cicco, M. Berrettoni, S. Stizza, E. Bonetti and G. Cocco, Phys. Rev. B **50**, 12386 (1994).
[44] X. Zhu, R. Birringer, U. Herr and H. Gleiter, Phys. Rev. B **35**, 9085 (1987).
[45] A. Higginbotham, *et al.* High Energy Density Phys. **5**, 44 (2009).
[46] Generally the DWF has contributions from both the configurational disorder (static) and thermal disorder (dynamic). The static contribution has been shown to be negligible in either nanocrystalline Fe [43, 44] or shock-compressed Fe [45] because the interfacial regions do not have any short-range order. Therefore the DWF in Fe EXAFS data is dominated by the thermal contribution.
[47] G. R. Fowles, J. Appl. Phys. **32**, 1475 (1961).
[48] R. F. Smith, *et al.* J. Appl. Phys. **110**, 123515 (2011).
[49] G. I. Taylor, H. Quinney, Proc. R. Soc. A **143**, 307 (1934).
[50] D. Rittel, G. Ravichandran and A. Venkert, Mater. Sci. Eng. A **432**, 191 (2006).
[51] G. H. Miller, E. I. Moses and C. R. Wuest, Opt. Eng. (Bellingham, Wash.) **43**, 2841 (2004).